

Mössbauer Spectroscopy

E. Gramowski* and M. Polaski

University of Minnesota, Minneapolis, MN, USA

(Dated: May 9, 2025)

We investigate the hyperfine interactions in elemental iron and Fe_3O_4 via Mössbauer spectroscopy using a ^{57}Co radioactive source. Gamma rays of 14.4 keV, emitted during the decay to ^{57}Fe , are resonantly absorbed by ^{57}Fe nuclei in the sample through the recoil-free Mössbauer effect. The hyperfine interactions cause small perturbations in the excitation energy of ^{57}Fe . A linear motor introduces Doppler shifts in the source energy, allowing high-resolution scans of the absorption spectrum. We were unable to collect data displaying the Mössbauer spectrum. Trials with and without a target material yielded nearly identical results suggesting a lack of absorption. Attempts to extract meaningful parameters were unsuccessful. We analyzed sample data by performing a Lorentzian fit to extract center peak values. These values were used to extract the hyperfine parameter values from a system of equations of the transition energies. We measure the isomer shift as $\epsilon_{\text{Fe}_3\text{O}_4} = 30.31 \pm 1.45$ neV, the quadrupole splitting as $\delta_{\text{Fe}} = 1.226 \pm 0.555$ neV and $\delta_{\text{Fe}_3\text{O}_4} = 1.635 \pm 0.771$ neV, and the magnetic hyperfine parameters as $g_0 = 190.11 \pm 1.46$ neV, $g_1 = 106.17 \pm 0.76$ neV for Fe, and $g_0 = 258.0 \pm 1.7$ neV, $g_1 = 148.62 \pm 1.19$ neV for Fe_3O_4 . These values lie within 1–2.5 σ of accepted literature values, with reduced chi-squared values of $\chi^2_\nu = 1.34$ for Fe and $\chi^2_\nu = 2.65$ for Fe_3O_4 , indicating statistically meaningful fits.

I. INTRODUCTION

Mössbauer spectroscopy is a powerful technique for probing the local electronic and magnetic environments of nuclei in solids. Discovered by Rudolf Mössbauer in 1958, it exploits the recoil-free emission and absorption of gamma rays by atomic nuclei bound within a crystal lattice.

As shown in figure 1, small perturbations in the atomic energy levels of ^{57}Fe isotopes within iron compounds provide information about local

electron density, electron symmetry, and internal magnetic field. The hyperfine structure of elemental iron leads to a characteristic six peak Mössbauer spectrum[4] 1.

In addition to elemental iron, which does not display isomer shifts due to the lack of oxygen, our study focuses on the hyperfine interactions in Fe_3O_4 , a mixed-valence iron oxide containing both Fe^{2+} and Fe^{3+} . This compound exhibits two distinct iron environments: tetrahedrally coordinated A sites occupied exclusively by Fe^{3+} , and octahedrally coordinated B sites shared by both oxidation states [4, 5]. These

* Communicating author

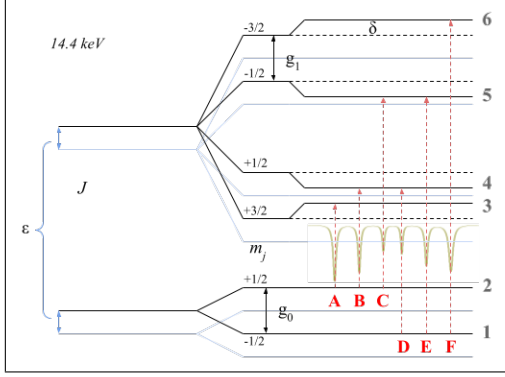


FIG. 1. Transition energies for ^{57}Fe . Energy level shifts due to quadrupole splitting (δ), isomer shift (ϵ), and magnetic hyperfine splitting ($g_{0,1}$) are shown with characteristic sextet Mössbauer spectrum (see theory C.).

distinct environments lead to separate sextets in the Mössbauer spectrum. However, due to line overlap at room temperature, we expect to observe nine peaks rather than twelve [5].

Our goal is to extract the isomer shift, quadrupole splitting, and magnetic hyperfine splitting from the Mössbauer spectrum of Fe_3O_4 using Lorentzian peak fitting and a linearized system of equations based on a system of equations representing the transition energies.

Beyond Fe_3O_4 , this methodology is broadly applicable to both terrestrial and extraterrestrial materials. For instance, miniaturized Mössbauer spectrometers have been deployed on NASA's Mars Exploration Rovers to study iron-bearing minerals [2], and similar instruments have been proposed for upcoming astrobiological missions to Europa [3].

To perform high-resolution spectroscopy, we

use a ^{57}Co source that decays to ^{57}Fe , emitting 14.4 keV gamma rays. The source is mounted on a linear motor driven by a sawtooth waveform. The motor accelerates the source at 149.20 mm/s^2 per 1/14 second cycle, introducing precise Doppler shifts on the order of μeV , which allows us to scan the nuclear resonance with fine energy resolution.

II. THEORY

The foundation of Mössbauer spectroscopy lies in the recoil-free emission and absorption of gamma rays by nuclei bound in a solid lattice [6]. The hyperfine interactions cause perturbations in the nuclear transition energy on the order of μeV . Energy loss due to lattice recoil,

$$E_{\text{recoil}} = \frac{(E_\gamma)^2}{2m_{\text{Fe}}c^2}, \quad (1)$$

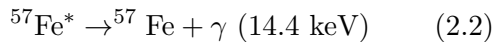
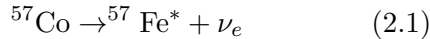
is on the order of meV and would otherwise obscure the fine structure induced by hyperfine effects. Recoil-free processes preserve energy resolution by eliminating this loss, allowing the absorbed and emitted photons to have matching energies. This high resolution enables the observation of hyperfine interactions.

To scan the absorption profile surrounding E_γ , the Doppler effect is used to introduce small energy shifts in the gamma rays via motion of the source. The Doppler energy shift is given by:

$$\Delta E_s = \left(\frac{v_0}{c}\right) E_\gamma, \quad (2)$$

where v_0 is the relative velocity between source and absorber. By systematically varying v_0 , we scan across the hyperfine spectrum.

We use a ^{57}Co source, which decays to an excited state of ^{57}Fe via electron capture. The excited nucleus then emits a gamma ray of 14.4 keV upon relaxation:



This transition is ideal for Mössbauer spectroscopy because the emitted photon energy matches the excitation energy of ^{57}Fe in the absorber.

A. Isomer Shift

The isomer shift arises from differences in s-electron density at the nucleus between the source and absorber [1]. Because s-electrons have non-zero probability density at the nucleus, small differences in the nuclear charge radius between the ground and excited states result in measurable energy shifts [4, 6]. These shifts alter the energies of the nuclear states unequally, producing a net change in the transition energy. In the Mössbauer spectrum, this appears as a uniform shift of the resonance peak [7], as illustrated in Fig. 2.

In Fe_3O_4 , the isomer shift is useful for distinguishing the two iron oxidation states. A sites are occupied by Fe^{3+} ions in tetrahedral coordination, while B sites contain a mixture of Fe^{2+}

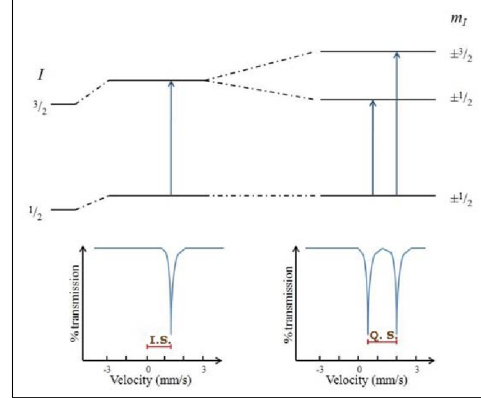


FIG. 2. Perturbations to transition energies and associated Mössbauer spectrum features arising from isomer shifts and quadrupole splitting [7].

and Fe^{3+} in octahedral coordination [4]. Because the isomer shift reflects the local electron density—affected by oxidation state and bonding environment—these ions exhibit distinct values of ϵ [5].

B. Quadrupole Splitting

Quadrupole splitting arises from the interaction between the nuclear quadrupole moment and an electric field gradient (EFG) at the nucleus. While a spherically symmetric environment produces no EFG, asymmetries in the surrounding charge distribution, such as lattice distortions or anisotropic bonding, lead to a non-zero gradient [4, 6, 7]. If the nucleus itself is non-spherical, this interaction modifies the energy levels of states with $J > 1/2$, producing sublevel shifts dependent on their orientation.

The energy shift is quantified by:

$$\delta = qe^2Q \frac{3m_J^2 - J(J+1)}{4J(2J-1)}, \quad (3)$$

where Q is the nuclear quadrupole moment, q is the EFG, J is the nuclear spin, and m_J is the magnetic quantum number [4, 5]. The result is a symmetric doublet in the Mössbauer spectrum, with splitting proportional to the magnitude of the EFG (see Fig. 2, 3).

C. Magnetic Hyperfine Splitting

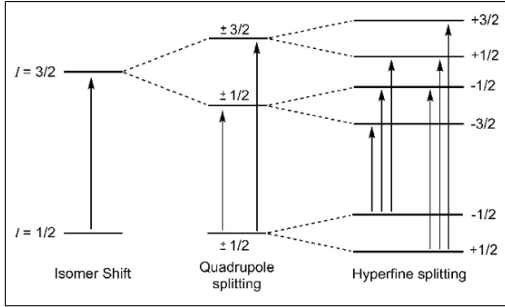


FIG. 3. Effects of hyperfine interactions on energy levels and their manifestations in Mössbauer spectra [7].

Magnetic hyperfine splitting occurs when the nuclear magnetic dipole moment interacts with a magnetic field at the nucleus. This internal field often arises from unpaired electron spins in magnetically ordered materials. The interaction causes Zeeman splitting of nuclear levels.

In ^{57}Fe , the Mössbauer transition occurs between an excited state with spin $J = 3/2$ and a ground state with $J = 1/2$. In the presence of a magnetic field, these states split into $2J + 1$ sublevels (Fig. 3). Allowed transitions satisfy

the selection rule $\Delta m = 0, \pm 1$, resulting in six absorption lines—a sextet.

The shift in energy for each sublevel is given by:

$$\Delta E = g_J m_J \mu_N B, \quad (4)$$

where g_J is the Landé g -factor, m_J is the magnetic quantum number, μ_N is the nuclear magneton, and B is the internal magnetic field. By measuring the spacing between lines, the magnitude of the hyperfine field can be extracted if the g -factors are known.

In Fe_3O_4 , both A-site (Fe^{3+}) and B-site ($\text{Fe}^{2+}/\text{Fe}^{3+}$) iron atoms contribute to the internal field, producing overlapping sextets. Due to slight differences in hyperfine fields and partial overlap of transitions, the observed spectrum typically contains nine peaks. These splittings reveal insight into the magnetic ordering and local field strengths at distinct crystallographic sites.

D. Hyperfine Structure and Parameter Relationships

The magnetic hyperfine interaction causes the nuclear states to split in a magnetic field B into Zeeman sublevels. For the ^{57}Fe transition from an excited state with spin $I_e = 3/2$ to a ground state with $I_g = 1/2$, this results in six allowed magnetic dipole transitions, governed by the selection rule $\Delta m = 0, \pm 1$.

The energy shift of each transition can be

written as:

$$\Delta E_i = (m_g g_0 - m_e g_1) \mu_N B + \epsilon \pm \delta,$$

where g_0 and g_1 are the Landé g -factors for the ground and excited states, m_g and m_e are their magnetic quantum numbers, μ_N is the nuclear magneton, B is the internal magnetic field at the nucleus, ϵ is the isomer shift, and δ represents the quadrupole splitting.

In the absence of a known magnetic field value, the expression is often recast into a system of linear equations where the observed transition energies are fitted directly in terms of g_0 , g_1 , ϵ , and δ [6]. For the six allowed transitions, this yields [1]:

$$\Delta E_1 = \left(\frac{1}{2}g_0 - \frac{3}{2}g_1\right) + \epsilon - \delta$$

$$\Delta E_2 = \left(\frac{1}{2}g_0 - \frac{1}{2}g_1\right) + \epsilon + \delta$$

$$\Delta E_3 = \left(\frac{1}{2}g_0 + \frac{1}{2}g_1\right) + \epsilon + \delta$$

$$\Delta E_4 = \left(-\frac{1}{2}g_0 - \frac{1}{2}g_1\right) + \epsilon + \delta$$

$$\Delta E_5 = \left(-\frac{1}{2}g_0 + \frac{1}{2}g_1\right) + \epsilon + \delta$$

$$\Delta E_6 = \left(-\frac{1}{2}g_0 + \frac{3}{2}g_1\right) + \epsilon - \delta$$

These equations form the basis for extracting hyperfine parameters from the spectrum using least-squares fitting. Because each energy difference corresponds to a known pair of m_g and m_e , the system is overdetermined and can be solved to high precision, provided the individual transitions are well-resolved.

III. EXPERIMENTAL SETUP

We mount the ^{57}Co source, which emits 14.4 keV gamma rays, to the ASA MOD K3 linear motor. The motor is driven by the ASA S600 Mössbauer controller via a feedback loop. The drive signal is a square wave that triggers the motor motion, while the velocity signal is a triangular waveform, indicating linear acceleration and symmetric oscillation of the source (Figure 4).

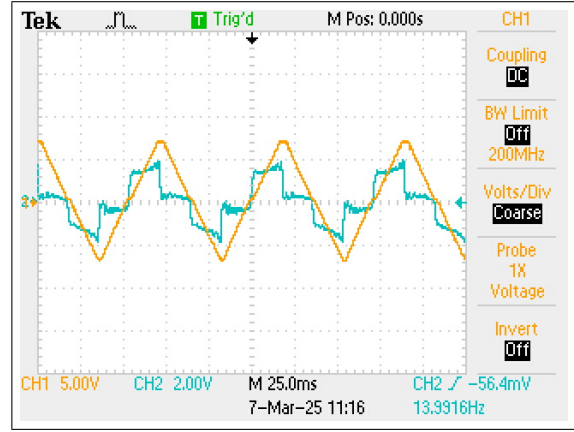


FIG. 4. Velocity signal (yellow) and drive signal (teal).

A function generator (HP-33120A) provides a 14 Hz triangle wave reference to the S600 driver. This frequency is chosen because it closely matches the natural frequency of the spring-mounted linear motor, allowing for stable resonance. The driver modulates the source's velocity to apply the Doppler effect, enabling fine control of the gamma-ray energy across the absorption spectrum.

The velocity signal is routed to a Stanford

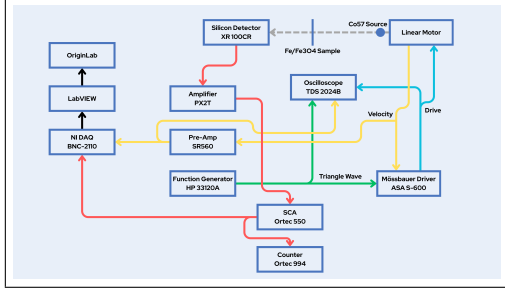


FIG. 5. Visualization of the Mössbauer apparatus, with appropriate equipment labeled [1].

Research Systems SR560 low-noise preamplifier. The amplified signal is digitized using a National Instruments BNC-2110 DAQ interface and a PCI-6036E card, which pass the data to a computer running a custom LabVIEW program.

Gamma rays emitted by ^{57}Fe nuclei in the absorber are detected by an Amptek XR-100CR silicon detector (Figure 5). For mid- to low-energy gamma rays (1–30 keV), the photoelectric effect dominates in silicon. A photoelectron absorbs the full gamma-ray energy, generating electron-hole pairs as it travels through the crystal. An applied electric field collects these charges, producing a current pulse proportional to the gamma-ray energy [8, 9].

This pulse is first amplified by the Amptek PX2T, which also supplies power to the detector. The signal is then sent to an Ortec 550 single-channel analyzer (SCA), which applies upper and lower energy thresholds to isolate events within a specified window. Only pulses corresponding to the 14.4 keV transition fall within this window; all others are rejected. The SCA,

set to internal (INT) mode, outputs a TTL logic pulse for accepted events. This pulse triggers both the Ortec 994 counter and the LabVIEW data acquisition system.

The Ortec 994 counter is used only during setup to confirm that the SCA output corresponds to the expected ^{57}Co gamma spectrum. However, it is not used for data collection due to its high sensitivity to electromagnetic interference and inability to continuously log data over long timescales [1]. Since data collection spans five days, counts must be recorded digitally. The custom LabVIEW program continuously logs both the energy of detected gamma rays and the velocity of the moving source.

IV. PROCEDURE

The gain setting of the PX2T amplifier directly influences the position and width of the spectral peaks observed by the detector. To ensure accurate peak resolution, the signal amplification is adjusted to ensure that the 14.4 keV peak remains within the measurable voltage range of the SCA (approximately 0 to 7.6 V), balancing adequate signal gain with proper threshold alignment. Excessive gain may shift the 14.4 keV peak out of the measurable range, whereas insufficient gain may result in poor peak resolution.

Before adjusting the SCA thresholds, we examine the ^{57}Co energy spectrum using an Ortec EASY-MCA multi-channel analyzer (MCA)

(Fig. 6). This analysis allows us to identify the location of the 14.4 keV Mössbauer peak and distinguish it from higher-energy gamma lines (e.g., near 122 keV and 136 keV). From this spectrum, we determine the approximate voltage corresponding to the 14.4 keV peak, which is necessary for setting the lower and upper energy thresholds on the SCA. Without this reference, the SCA window could be improperly positioned, either excluding the Mössbauer signal or including background noise from unrelated transitions. To ensure the SCA works with the detector, we measure counts across the ^{57}Co spectrum using the ORTEC counter and SCA (figure 12).

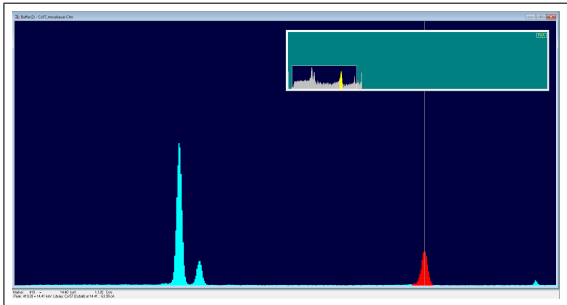


FIG. 6. MCA acquired ^{57}Co spectrum in Maestro. Highlighted is the 14.4 keV peak

We adjust the SCA thresholds to align with the expected based on the labeling of the source shield and reference spectra available in the literature. The PX2T output is connected to the Ortec 550 SCA, which is routed to the Ortec 994 counter. Using this setup, we verify that the SCA output (see figures 13) responds predominantly to events associated with the 14.4 keV peak. To ensure precision, we connect the SCA

to the DAQ and use a custom LabVIEW program to record the area around the 14.4 keV peak. We then plot the data in Origin and fit it to a Gaussian to extract a center value for the SCA window 14. This ensures that subsequent counts recorded during data acquisition correspond to resonant absorption and are not contaminated by background gamma emissions from other decay branches.

V. DATA ANALYSIS

Data analysis of sample data begins with background subtraction to remove non-resonant gamma counts. We fit the transmission spectrum using Lorentzian functions, which are appropriate because the natural line shape of nuclear gamma-ray transitions, governed by the Heisenberg uncertainty principle, is Lorentzian [1, 6]. We then extract the hyperfine parameters for the isomer shift (in Fe_3O_4 only), quadrupole splitting, and hyperfine splitting using a custom Python script.

A. Peak Fitting

We first analyze the Mössbauer transmission spectrum for elemental Fe. The spectrum displays the expected six-peak absorption pattern, although it initially includes edge noise (see Appendix, Fig. 11) and a systematic quadratic curvature due to imperfections in the velocity drive system [1], as seen in the first plot in Fig. 7.

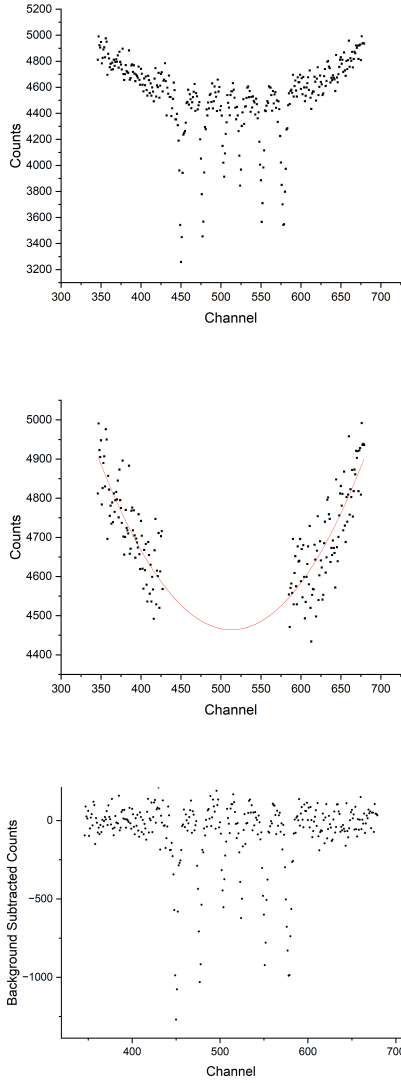


FIG. 7. In order: Data just after subtraction of edge noise, quadratic fit applied to data without peaks, linearized spectrum.

We remove the unreliable edge channels and fit a second-degree polynomial to the off-peak regions using Origin’s masking feature to exclude the peaks (Fig. 7, plot 2). This polynomial models the non-resonant background, which we subtract from the raw data to isolate the resonant absorption features. After subtraction, we re-

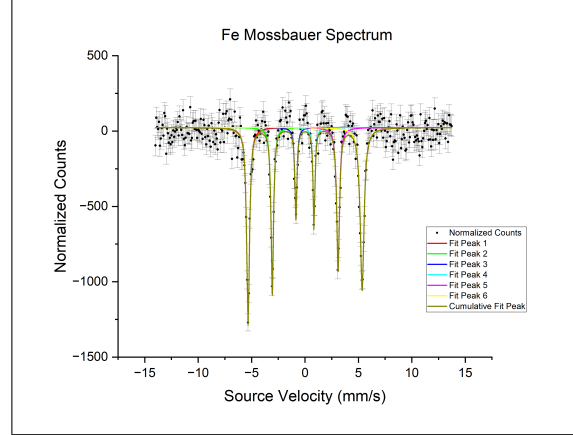


FIG. 8. Fe spectrum after peak fitting and background subtraction.

store the center peak region and prepare to extract peak centers from the linearized spectrum (Fig. 7, plot 3).

With the background removed, we fit the spectrum using Origin’s multiple Lorentzian peak fitting utility. We manually place initial peak positions and constrain their widths and separations based on known nuclear transition rules. The fitting algorithm refines the parameters automatically, and we apply error weighting using the propagated uncertainties. This procedure yields the final transmission spectrum for elemental iron (Fig. 8).

We repeat this process for the Fe_3O_4 sample. The initial spectrum also exhibits a strong central feature and mild curvature, which we remove using the same quadratic subtraction and Lorentzian peak fitting workflow. The result is a resolved eight-line spectrum corresponding to both A-site and B-site contributions from Fe_3O_4 (figure 9). We are unable to resolve a ninth peak,

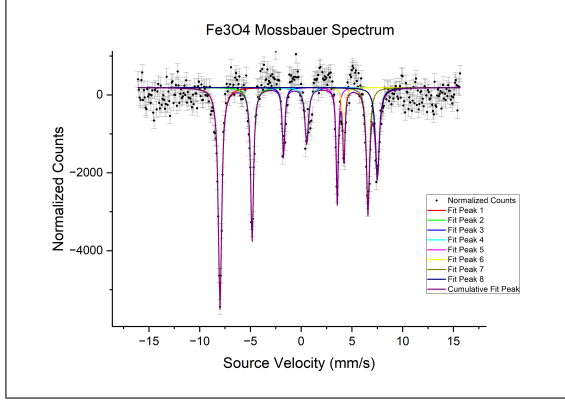


FIG. 9. Fe_3O_4 spectrum after peak fitting and background subtraction.

likely due to limited counts in the provided data.

To convert the Lorentzian peak centers from channel number to Doppler velocity, we calibrate the energy axis using the known outermost peak separation of elemental iron. The accepted value for this separation is 10.657 mm/s. By dividing this velocity range by the measured channel separation between the outermost peaks, we determine a linear conversion factor in mm/s per channel. This factor is then applied to the fitted peak centers in both the Fe and Fe_3O_4 spectra.

The resulting Doppler velocities v are converted into transition energy shifts using the first-order Doppler relation:

$$\Delta E = \left(\frac{v}{c}\right) E_\gamma, \quad (5)$$

where $E_\gamma = 14.4 \text{ keV}$ is the transition energy and c is the speed of light. These energy shifts represent the six allowed magnetic dipole transitions in ^{57}Fe and are used to extract the hyperfine interaction parameters as described in the Theory section.

B. Hyperfine Parameter Extraction

We then extract the hyperfine interaction parameters from the fitted Doppler shifts. The six allowed transitions in ^{57}Fe arise from combinations of nuclear sublevels governed by magnetic and electric hyperfine interactions. The theoretical model describing these transitions is presented in the Theory section.

To extract the hyperfine parameters g_0 , g_1 , ϵ , and δ , we implement a custom Python script that ingests the transition energies calculated from the Lorentzian peak centers. The script defines the symbolic form of each transition energy based on quantum number assignments and uses SymPy to represent the system analytically. These symbolic expressions are then evaluated numerically using the energy shifts derived from the Doppler-transformed velocities.

The system is overdetermined, so we solve it using linear least-squares regression, ensuring that all six observed transitions contribute to the determination of each parameter. The script outputs the best-fit values for the hyperfine parameters, along with their associated uncertainties derived from the covariance matrix of the regression. This method provides a robust and consistent means of extracting spectroscopic quantities from the experimental data, ensuring that the final values reflect the combined effects of magnetic and electric hyperfine interactions observed in the Fe and Fe_3O_4 spectra.

VI. RESULTS

Despite repeated efforts, we are unable to collect meaningful data from either elemental Fe or Fe_3O_4 . In total, we conduct several hundred-hour acquisition trials, yet runs performed with and without a target produce nearly identical results (figure 10). This suggests that absorption features are either obscured by a dominant central spike or that absorption is entirely absent, likely due to misalignment or ineffective sample placement.

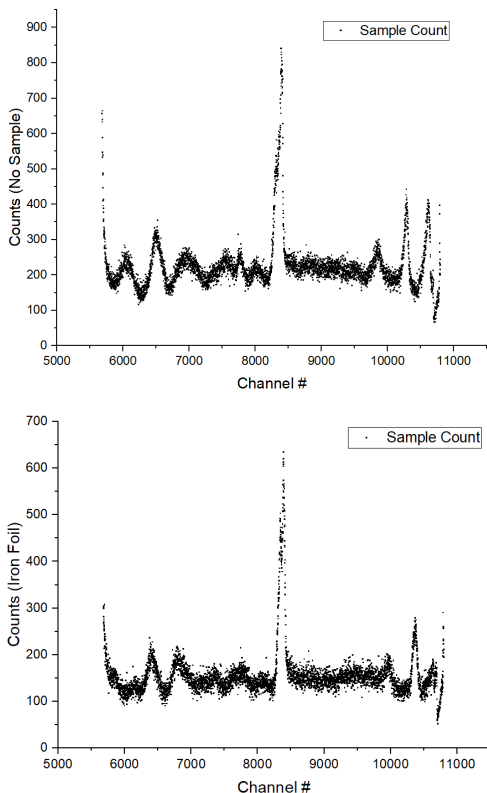


FIG. 10. Raw Mössbauer spectra. Top: data with no absorber present. Bottom: data with Fe foil.

Initial documentation provided by Kurt Wick on the course website suggests that the source

may be positioned too close to the absorber. In response, we adjust the source-to-sample distance in 5 cm increments, moving it back by a total of 25 cm. Each position is tested over a one-hour acquisition period. While these adjustments reduce the overall count rate, they produce no qualitative change in spectral shape. We next vary the lateral placement of the absorber between the source and the detector, but this also yields no improvement.

Finally, we introduce lead collimators between the source and sample to limit the angular spread of incident gamma rays and better direct them toward the absorber. The resulting spectra are shown in Fig. 9. Due to a malfunctioning linear actuator that halted data acquisition for over a month, we are ultimately unable to recover meaningful spectral data from our own experimental runs. Consequently, we proceed with analysis using provided sample data.

We evaluate the quality of our Mössbauer spectral fits using the reduced chi-squared statistic χ^2_ν , which measures the goodness-of-fit while accounting for the number of data points and fit parameters. A value of $\chi^2_\nu \approx 1$ indicates that the fit is consistent with the estimated statistical uncertainty.

For elemental iron, we obtain a reduced chi-squared of $\chi^2_\nu = 1.3405$, indicating a high-quality fit with minimal residual structure. The extracted hyperfine parameters are $g_0 = 190.11 \pm 1.46$ neV, $g_1 = 106.17 \pm 0.76$ neV, and quadrupole splitting $\delta = 1.23 \pm 0.56$ neV. The

isomer shift is fixed at zero, since elemental iron is used as the calibration reference. Comparing these to accepted literature values of $g_0 = 188 \pm 0.38 \text{ neV}$ and $g_1 = 108 \pm 0.24 \text{ neV}$ [1], we find that our measured g_0 is within 1.5σ of the expected value, and our measured g_1 is within 2.4σ . The quadrupole splitting is small, as expected for elemental iron, and consistent with second-order hyperfine effects.

For Fe_3O_4 , the reduced chi-squared increases to $\chi^2_\nu = 2.6464$, indicating the presence of larger residuals than expected from statistical noise alone. This may be attributed to several factors including peak broadening, partially overlapping transitions, and possible effects of electronic relaxation at room temperature [4, 5]. Nonetheless, the fit converges well, and the extracted hyperfine parameters are $g_0 = 258.0 \pm 1.7 \text{ neV}$, $g_1 = 148.62 \pm 1.19 \text{ neV}$, quadrupole splitting $\delta = 1.635 \pm 0.771 \text{ neV}$, and isomer shift $\epsilon = 30.31 \pm 1.45 \text{ neV}$. Literature values for stoichiometric Fe_3O_4 report $g_0 = 269 \pm 13.4 \text{ neV}$, $g_1 = 155 \pm 8.6 \text{ neV}$, and isomer shift $\epsilon = 26.9 \pm 6.7 \text{ neV}$ [1]. Our measured g_0 lies within 0.8σ of the literature value, g_1 within 0.7σ , and the isomer shift within 0.5σ . The quadrupole splitting is again small but clearly resolved, with no significant deviation from the expected null value.

Taken together, these results demonstrate that our fitted hyperfine parameters are statistically consistent with established Mössbauer values for both elemental iron and Fe_3O_4 . The low sigma deviations and reasonable chi-squared val-

ues confirm that our spectral models capture the key physical interactions in both samples.

VII. CONCLUSION

Although our experimental apparatus was unable to produce usable Mössbauer spectra due to persistent mechanical limitations and an overall lack of gamma ray absorption, we successfully performed a full analysis on provided transmission spectra for both elemental iron and Fe_3O_4 . Background subtraction and Lorentzian peak fitting allowed us to identify transition energies with high resolution. Calibration using a known reference standard enabled conversion from channel number to Doppler velocity, and subsequently to energy shifts.

Using these shifts, we extracted the hyperfine parameters g_0 , g_1 , ϵ , and δ through a symbolic least-squares regression implemented in Python. For elemental iron, our results show excellent agreement with literature values, particularly for the magnetic hyperfine splitting. In the case of Fe_3O_4 , the observed eight-peak spectrum and extracted parameters are consistent with expectations for mixed-valence iron oxides, including clearly resolved quadrupole shifts. Two of the three isomer shifts were well characterized, the other was obscured due to a lack of data points in the provided sample data.

These results confirm the viability of Mössbauer spectroscopy as a sensitive probe of magnetic and electronic structure in iron-

containing compounds. While hardware limitations prevented us from collecting original data, our computational analysis demonstrates the full workflow from transmission spectrum to extracted hyperfine parameters and support the validity of the methodology for future investigations.

-
- [1] Wick, K. Pfeifer, C. "Methods of Experimental Physics (MXP) - Moessbauer Effect Lab", 2013
- [2] Blumers, M. et al, "The miniaturized Mossbauer spectrometer MIMOS IIA: Increased sensitivity and new capability for elemental analysis", 2010
- [3] Schröder, C., Klingelhöfer, G., Bailey, B. E., Staudigel, H. (2005). Mössbauer spectroscopy as a tool in astrobiology. *ICAME 2005*, 567–571.
- [4] Westerdale, S. "Mossbauer Spectroscopy of ^{57}Fe ", 2010
- [5] Preston, R. S. Hanna, S. S. "Mössbauer Effect in Metallic Iron", 1962
- [6] Mössbauer, R. L. "Nuclear Resonance Fluorescence of Gamma Radiation in Iridium.", 1958
- [7] Kurian, R. (2011). *First principles theoretical modeling of the isomer shift of Mossbauer spectra*. s.n.
- [8] Henke, B. L., Gullikson, E. M., Davis, J. C. (1993). X-ray interactions: Photoabsorption, scattering, transmission, and reflection at $E=50\text{--}30000\text{ eV}$, $Z=1\text{--}92$. *Atomic Data and Nuclear Data Tables*, 54(2), 181–342. <https://doi.org/10.1006/adnd.1993.1013>
- [9] Amptek. (n.d.). XR-100CR Si-PIN x-ray detector. Amptek. Retrieved March 7, 2025, from <https://www.amptek.com/internal-products/xr-100cr-si-pin-x-ray-detector>
- [10] Chechev, V.P. Kuzmenko, N.K. "LNHB/CEA Table de Radionucléides - Co-57", 2017

Sample	I. S. (ϵ)	Q.S. (δ)	g_0	g_1
Fe ($r\chi^2 = 1.34053$)	—	1.226 ± 0.555	190.11 ± 1.46	106.174 ± 0.757
Fe ₃ O ₄ ($r\chi^2 = 2.64638$)	30.31 ± 1.45	1.635 ± 0.771	258.0 ± 1.7	148.62 ± 1.19

TABLE I. Extracted Mössbauer parameters for elemental Fe and Fe₃O₄, in units of nano-electronvolts (neV)

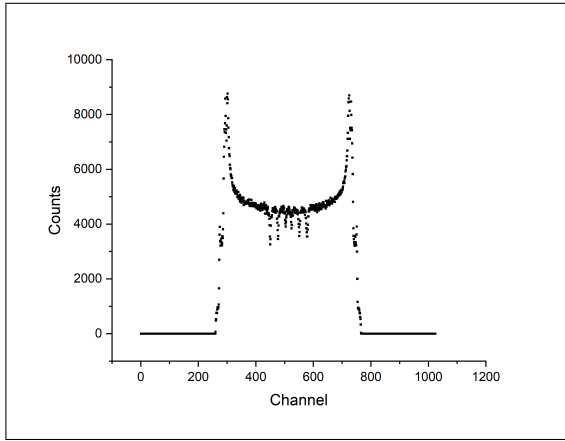


FIG. 11. sample Fe raw data before analysis.

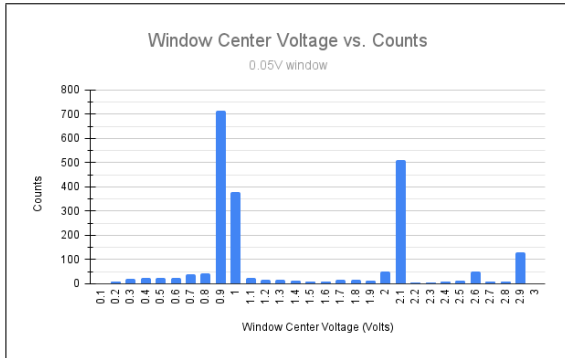


FIG. 12. ^{57}Co spectrum data collected using ORTEC counter.

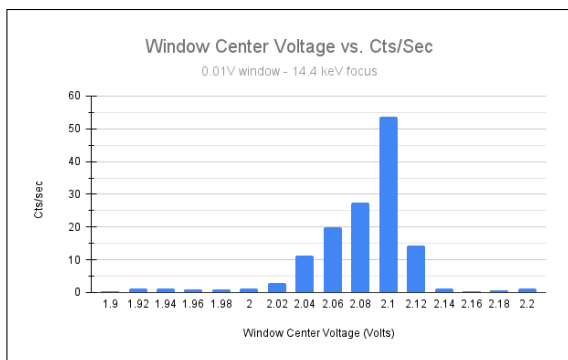


FIG. 13. High resolution scan of 14.4 keV peak collected with ORTEC counter.

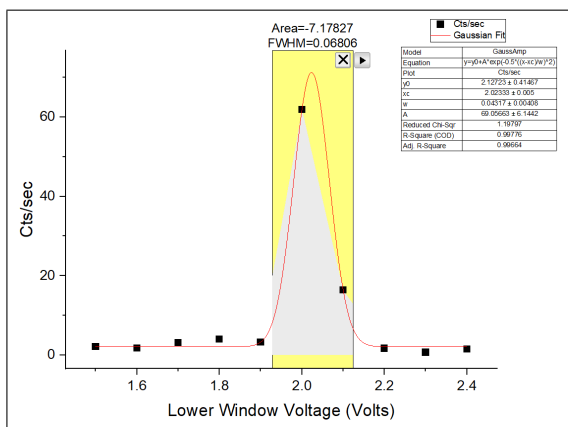


FIG. 14. SCA window size calibration data, fit to Gaussian using Origin.